

Investigation into the Use of a Lead Slowing-Down Spectrometer for Neutron Cross  
Section Analysis

By  
Jackson Keppen

A THESIS

submitted to

Oregon State University  
University Honors College

in partial fulfillment of  
the requirements for the  
degree of

Honors Baccalaureate of Science in Nuclear Engineering  
(Honors Scholar)

Presented May 15, 2018  
Commencement June 2018



## AN ABSTRACT OF THE THESIS OF

Jackson Keppen for the degree of Honors Baccalaureate of Science in Nuclear Engineering presented on May 15, 2018. Title: Investigation into the Use of a Lead Slowing-Down Spectrometer for Neutron Cross Section Analysis

Abstract approved:

---

Todd Palmer

A lead slowing-down spectrometer (LSDS) was modeled in the hopes of beginning a nuclear data development campaign at Oregon State University. An LSDS can be used for neutron interrogation techniques, such as determining isotopic inventory of a sample of unknown components or determining the cross section of a sample of known components. The purpose of this research was to determine the flux profile of a neutron pulse within the LSDS over time and determine the effectiveness of the LSDS for neutron cross section analysis. In order to do this, Monte Carlo N-Particle simulations were used to model the LSDS along with the shielding, detectors, and the room surrounding the device. A variety of different room configurations, shielding, and samples were placed into the model to determine how the coefficients that describe the operation of the LSDS change. The resulting data was a normal-shaped probability distribution function centered at the most abundant neutron energy that can be used to determine the cross section of a sample with about  $\pm 30\%$  accuracy, which corresponds to the width of the distribution function. Changes to the system caused the coefficients of the LSDS to change by approximately 12% on average, indicating that the flux spectrum within the device is relatively stable regardless of the environment and sample. The modeled irradiation resulted in cross sections with an error relative to the established data ranging from 66.1% to 2990%.

Key Words: neutron, cross-section, radiation transport

Corresponding e-mail address: keppenj@oregonstate.edu

©Copyright by Jackson Keppen  
June 8, 2018  
All Rights Reserved

Investigation into the Use of a Lead Slowing-Down Spectrometer for Neutron Cross  
Section Analysis

By  
Jackson Keppen

A THESIS

submitted to

Oregon State University  
University Honors College

in partial fulfillment of  
the requirements for the  
degree of

Honors Baccalaureate of Science in Nuclear Engineering  
(Honors Scholar)

Presented May 15, 2018  
Commencement June 2018

Honors Baccalaureate of Science in Nuclear Engineering project of Jackson Keppen  
presented on May 15, 2018

APPROVED:

---

Todd Palmer, Mentor, representing Oregon State's School of Nuclear Science and Engineering

---

Dan LaBrier, Committee Member, representing Oregon State's School of Nuclear Science and Engineering

---

Haori Yang, Committee Member, representing Oregon State's School of Nuclear Science and Engineering

---

Toni Doolen, Dean, Oregon State University Honors College

I understand that my project will become part of the permanent collection of Oregon State University Honors College. My signature below authorizes release of my project to any reader upon request.

---

Jackson Keppen, Author

# Contents

<b>1</b>	<b>Introduction</b>	<b>1</b>
1.1	Nuclear Data . . . . .	1
1.2	Methods of Developing Cross Sections . . . . .	1
<b>2</b>	<b>The LSDS</b>	<b>3</b>
2.1	History and Development . . . . .	4
2.2	Physics and Theory . . . . .	5
2.3	Detectors . . . . .	8
2.4	Operation of the LSDS . . . . .	9
<b>3</b>	<b>Monte Carlo Model</b>	<b>10</b>
3.1	MCNP Basics . . . . .	10
3.2	Extracting Data . . . . .	11
3.3	The LSDS in MCNP . . . . .	11
<b>4</b>	<b>Methods</b>	<b>12</b>
4.1	Samples . . . . .	12
4.2	Determining the Cross Sections . . . . .	13
4.2.1	ENDF Data . . . . .	14
4.3	Poorly Resolved Region . . . . .	14
4.4	Flux Profile . . . . .	15
4.4.1	Determining $K$ and $t_0$ . . . . .	17
4.4.2	The Resolution Function . . . . .	19
4.5	Determining Count Rate . . . . .	20
4.6	Determining the Flux Normalization Factor . . . . .	20
<b>5</b>	<b>Results</b>	<b>22</b>
5.1	Cross Sections . . . . .	23
5.1.1	Case 1, Au-197 . . . . .	23
5.1.2	Case 2, Low Mass Au-197 . . . . .	24
5.1.3	Case 3, High Mass Au-197 . . . . .	25
5.1.4	Case 4, Moved Detector, Au-197 . . . . .	27
5.1.5	Case 5, Au-197 with $10^8$ Source Particles . . . . .	29
5.1.6	Case 6, U-238 . . . . .	30
5.1.7	Case 7, Tantalum . . . . .	32
5.1.8	Case 8, Nickel . . . . .	34
5.1.9	Case 9, Titanium . . . . .	35
5.1.10	Case 10, Chromium . . . . .	36
5.1.11	Case 11, O-16 . . . . .	37
5.1.12	Tabulated Results . . . . .	38
5.2	Shortcomings . . . . .	39

<b>6 Conclusion</b>	<b>40</b>
6.1 Future Work . . . . .	40

# 1 Introduction

There is a perpetual need to expand and improve nuclear data for national security, counter-proliferation, and a wide array of nuclear science endeavors. Certain isotopes of elements such as oxygen, uranium, and plutonium have poor data or are lacking data entirely. Other key isotopes critical to reactor design, such as tungsten and gadolinium have poorly resolved cross sections. Consequently, the Domestic Nuclear Detection Office (DNDO), a sub-agency of the Department of Homeland Security, is soliciting research to reduce the uncertainty in energy-dependent nuclear data [1]. At the same time, Pacific Northwest National Laboratory (PNNL) has a lead slowing-down spectrometer (LSDS) that could be available for the Oregon State University School of Nuclear Science and Engineering, provided a sufficiently strong neutron source can be procured [2]. Significant analysis is necessary to establish the characteristics of the LSDS, determine the required source for various applications, and to ensure that the device can be safely and effectively used. This thesis describes the initial probe into quantifying these characteristics of the LSDS.

## 1.1 Nuclear Data

Nuclear data represents empirically derived information that pertains to nuclear reactions and interactions. It includes decay constants for unstable isotopes, energy of decay products, and cross section data. In this case, the nuclear data of concern is the cross section of materials. A cross section represents the reaction probability between a particular type of radiation and a particular material [3]. Cross sections are dependent on the type of radiation, the energy of the radiation, and the material itself. A cross section is also dependent on the type of interaction that occurs. For our interests, there are inelastic and elastic scattering interactions, as well as neutron capture and fission reactions. These cross sections are used for nuclear engineering in a similar manner to how steam tables are used for thermodynamics, or how convective coefficients are used for heat transfer. The main goal of this research is to investigate the potential for an LSDS to refine these cross section values [4].

## 1.2 Methods of Developing Cross Sections

There are a variety of ways that neutron cross sections can be measured [5]. The most common method is the Time-Of-Flight (TOF) method. TOF generally relies on the non-relativistic energy and velocity relationship described as:

$$E = \frac{1}{2}mv^2, \tag{1}$$

where:  $E$  is energy,  $m$  is mass, and  $v$  is velocity.

All methods that measure neutron interaction require a neutron source. This can take the form of a reactor, a sub-critical pile, a fusion source, or any other method of generating neutrons. For TOF methods, the neutron energy is determined by measuring the amount of time that it takes for the neutrons to travel from the source to the target and then using

$$v = \frac{d}{t}, \quad (2)$$

where:  $d$  is distance and  $t$  is time.

The time that the neutrons are traveling is measured using a mechanism that can 'pulse' the neutrons. This mechanism could be as simple as a Fermi chopper, which is a rotating drum full of alternating plates of aluminum and cadmium [6]. When the cadmium plates are parallel to the neutron flux, the neutrons can pass through the chopper. An indicator is connected between the chopper and a timer so that when the chopper is in the 'open' position, the timer can start timing.

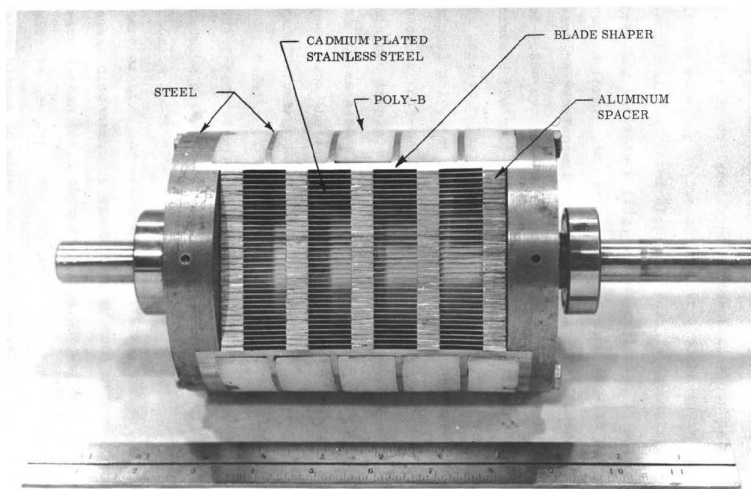


Figure 1: A Fermi Chopper  
[5]

The measured time is compared against the readout from a detector near the target, which is usually measuring the gamma rays coming off from the target. The gamma rays measured by the detector give an indication of the rate of the neutron interactions with the target. If the mass of the sample and the magnitude of the neutron flux are known, then a simple version of the reaction rate formula can be used,

$$RR = \eta\sigma\phi N, \quad (3)$$

where:  $RR$  is reaction rate of the target,  $\eta$  is detector efficiency,  $\sigma$  is the microscopic cross section, and  $N$  is the number density of the target.

Equation 3 needs to be re-arranged for the microscopic radiative capture cross section to determine the cross section of the target,

$$\sigma_a = \frac{RR}{\eta\phi N}. \quad (4)$$

Other techniques for determining cross sections are categorized as: beam transmission, in-pile, and activation [5]. Beam transmission is similar in form to the TOF method described previously, but it measures the attenuation of the neutron flux rather than the gamma rays emitted by an irradiated target. The beam transmission method measures the uncollided neutron flux, usually using a  $\text{BF}_3$  detector, and then measures the flux when a target is placed between the source and the detector. The cross section can then be determined by the change in flux as described by

$$\sigma_t = \frac{-\log \frac{I}{I_0}}{Nt}, \quad (5)$$

where:  $I_0$  is the initial flux intensity,  $I$  is the intensity with target, and  $t$  is the target thickness. A chopper can be used for beam transmission to measure the energy-dependence of the cross section. The beam transmission method determines the total cross section, as both scattering interactions and absorption interactions can impact the flux incident upon the detector.

The in-pile method uses a sample placed within the core of a reactor or sub-critical pile and the change in reactivity is measured. This method only accounts for the absorptive cross section. Perturbation theory can be used to compute the cross section in this case.

The activation method involves irradiating a material, and measuring the induced activity of it. This method only measures absorption reactions that result in radioactive isotopes.

## 2 The LSDS

Structurally, an LSDS is a pile composed of high purity ( $> 99.999\%$  pure) lead bricks that are arranged into a cube. For instance, the LSDS located at Los Alamos National Laboratory is a cube that is 1.2  $m$  along each side [7]. There are two slots in the LSDS: one is for inserting the sample and the other is for the neutron source. An array of detectors can be placed in and around the LSDS to monitor the neutron flux

and gamma ray production. An LSDS requires a neutron source to function, as it contains no fissile material or other inherent neutron sources. This source is pulsed, and the counts recorded on the detectors are measured as a function of time. The overarching concept is similar to the TOF method, but the LSDS relies on the time that the neutrons spend within its volume while the TOF method relies on the time that the neutrons spend traveling to the target.

The high purity lead is needed to maintain a consistent measurement profile. Small amounts of foreign material could be enough to disrupt the clarity of the output from the LSDS [8].

## 2.1 History and Development

The idea of a neutron spectrometer based on the principals of neutron slowing down time was quantified by Bergman et al. in 1955 [9]. The first use of the LSDS was for the “slowing-down-time” (sdt) method of neutron cross section analysis. Originally, the LSDS used a Penning type ion source to create deuterium-tritium fusion reactions to generate neutrons, and a proportional counter to indirectly measure the neutron yield by measuring the  $\alpha$  particles that were also created by the fusion reaction. The form of the LSDS has not changed significantly since its first inception, shown in Figure 2.

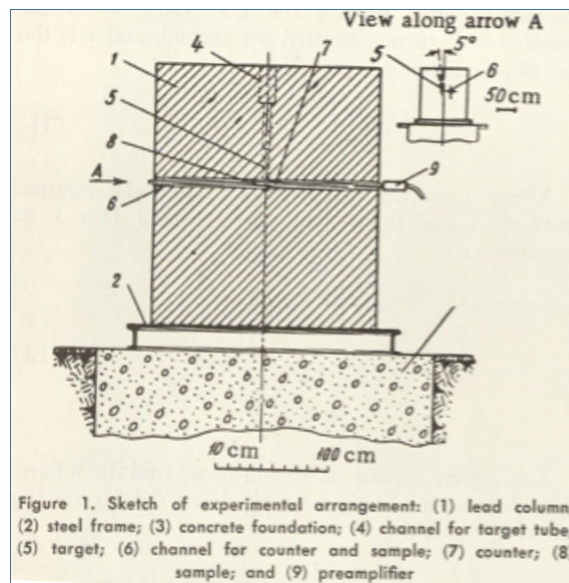


Figure 2: Sketch of LSDS [9]

The first investigations were into the cross sections of silver, zinc, manganese, cadmium, and copper [9]. The conclusion of their results were that the energy resolution

for the cross section was on the order of 30% in the  $eV$  to low  $keV$  range, but had a neutron flux intensity that was three to four orders of magnitude greater than TOF methods with similar sources. The increase in neutron flux intensity could be very important to looking at either low mass or low cross section samples [10].

The investigation into the use of an LSDS did not stop with Bergman's research. Similar efforts have been taken up at several other locations, particularly at Los Alamos National Laboratory (LANL) and Rensselaer Polytechnic Institute (RPI) [8, 7, 11]. At RPI, a team under Y. Danon has been exploring the use of an LSDS to determine cross sections using similar methods to Bergman [7]. They have focused particularly on the fission cross sections of heavier isotopes such as curium, einsteinium, and californium [11]. Y. Danon et. al has used the RPI 60  $MeV$  electron linear accelerator fired at a helium-cooled tantalum pile to produce neutrons within the LSDS. They reported a resolution of the neutron energy on the order of 35%, but were able to achieve a  $1\sigma$  error of approximately 10% in a sample of  $^{254}\text{Es}$  that only weighed 0.21  $\mu g$ .

## 2.2 Physics and Theory

A brief review of neutron slowing down time will be given to help develop a full understanding of the functioning of the LSDS. The basis of slowing down time is in neutron lethargy,

$$u = \log \frac{E_0}{E}, \quad (6)$$

where:  $u$  is the lethargy of neutrons at energy  $E$  and  $E_0$  is the initial neutron energy [3].

This can be rewritten as

$$u = \log E_0 - \log E,$$

and defining  $du$  as

$$du = \frac{-dE}{E}, \quad (7)$$

or

$$u_f - u_i = \Delta u = [\log(E_0) - \log(E_f)] - [\log(E_0) - \log(E_i)] = \log\left(\frac{E_i}{E_f}\right), \quad (8)$$

where:  $u_f$  is the final lethargy,  $u_i$  is the initial lethargy,  $E_f$  is the final energy, and  $E_i$  is the initial energy. The average neutron lethargy gain per collision, assuming elastic scattering, can be calculated by

$$\xi = 1 + \frac{\alpha}{1 - \alpha} \log \alpha, \quad (9)$$

where

$$\alpha = \left( \frac{A - 1}{A + 1} \right)^2$$

in which  $A$  is the atomic mass of the scattering medium. For high  $A$  materials such as lead, the average neutron lethargy gain per collision is very small, on the order of 0.01.

Consider that the scattering interaction rate is a function of scattering cross section and speed of the form

$$\omega = \Sigma_s v, \quad (10)$$

where:  $\omega$  is the frequency of scattering events,  $\Sigma_s$  is the scattering cross section, and  $v$  is the speed of the particles. The total number of interactions is the frequency of scattering events during a time interval  $\Delta t$ ,

$$R = \Sigma_s v \Delta t. \quad (11)$$

Since  $\xi$  is the lethargy gain per collision, and  $R$  is the total number of collisions, we can combine the two to yield the general slowing down equation of the form,

$$du = \xi \Sigma_s v dt. \quad (12)$$

Equation 12 describes the gain in neutron lethargy as a function of the material properties of the scattering medium, the neutron speed, and the time interval.  $\Delta t$  is also known as the slowing down time.

In the LSDS, the lethargy can be determined by the energy of the channel that contains the highest relative flux at a given time [11]. The energy of the highest relative flux, which is also the mean of the energy of the flux spectrum due to the Gaussian distribution, can be described as a function of time as seen in Equation 13,

$$\bar{E} = \frac{K}{(t + t_0)^2}, \quad (13)$$

where:  $\bar{E}$  is the average energy,  $K$  and  $t_0$  are constants depending on the materials, and  $t$  is the time after the pulse.  $K$  and  $t_0$  are derived in Section 4.4.1. Using Equation 13 to develop the energy, the gamma count rate measured in the detector can be attributed to that particular energy, allowing for energy dependent cross sections to be developed.

The count rate of gamma rays in the detector must be measured to determine the cross section [7]. The counts in channel  $i$  for sample  $x$ , as described by Danon, can be calculated by:

$$C_i^x = F\eta^x N^x \phi_r(E_i) \bar{\sigma}^x(E_i) \Delta E_i, \quad (14)$$

where:  $C_i^x$  represents the counts from sample  $x$  in channel  $i$ ,  $F$  is the flux normalization factor,  $\eta^x$  is the detector efficiency,  $N^x$  is the number of atoms of sample  $x$ ,  $E_i$  is the average energy of macrochannel  $i$ ,  $\phi_r(E_i)$  is the relative energy dependent flux,  $\bar{\sigma}^x(E_i)$  is the resolution-broadened cross section of sample  $x$  in channel  $i$ , and  $\Delta E_i$  is the width of channel  $i$  in energy units ( $\Delta E_i = E_{i+1} - E_i$ ) [11].

The spatial dependence of the neutron flux is not considered, as the sample has an identical position within the LSDS for every test.

$F$ , or the flux normalization factor, is an important quantity that acts as a calibration for the LSDS. The method of determining  $F$  is to rearrange the above equation to solve for  $F$ , and calibrate the LSDS with an isotope that has a well-defined cross section. In literature, the fission cross section of U-235 is typically used [11]. In this case, the  $(n, \gamma)$  reaction for Au-197 was used,

$$F = \frac{C_i^{197}}{\eta^{197} N^{197} \phi_r(E_i) \bar{\sigma}^{197}(E_i) \Delta E_i}, \quad (15)$$

where  $\bar{\sigma}^{197}(E_i)$  is the Au-197 broadened  $(n, \gamma)$  cross section, given by

$$\bar{\sigma}^{197}(E_i) = \frac{1}{\sqrt{E_i}} \int_{E_{min}}^{E_{max}} G(E, E_i) \sqrt{E} \sigma_\gamma^{197}(E) dE, \quad (16)$$

where:  $\sigma_\gamma^{197}(E)$  is the ENDF cross section for  $^{197}\text{Au}$ , and  $G(E, E_i)$  is the Gaussian resolution function of the LSDS.

The final flux normalization factor is the energy-dependent flux normalization factors averaged across all energy channels. When  $F$  is determined, the ENDF-equivalent cross section can be calculated by

$$\sigma(E_i) = \frac{1}{\eta^x N^x F \phi_r(E_i) \Delta E_i} C_i^x. \quad (17)$$

The broadened value for the cross section needs to be determined to solve for  $F$ . The trapezoid method was used to approximate the integral in Equation 16 [12]. The integration was evaluated by

$$\int_a^b f(x)dx \approx \int_a^b (a_0 + a_1x + \dots + a_nx^n)dx, \quad (18)$$

and after some manipulation, we approximate the integration of the function as

$$\int_a^b f(x)dx \approx (b - a)\frac{f(b) + f(a)}{2}, \quad (19)$$

where the integral being evaluated is

$$\frac{1}{\sqrt{E_i}} \int_{E_{min}}^{E_{max}} G(E, E_i) \sqrt{(E)} \sigma_x(E) dE,$$

so  $f(x) = G(E, E_i) \sqrt{(E)} \sigma_x(E)$ . This is put into Equation 19,

$$\bar{\sigma}_x(E_i) = \frac{1}{\sqrt{E_i}} * (E_{max} - E_{min}) * \frac{G(E_{max}, E_i) \sqrt{E_{max}} \sigma_x(E_{max}) + G(E_{min}, E_i) \sqrt{E_{min}} \sigma_x(E_{min})}{2} \quad (20)$$

This can be further discretized so that  $E_{min}$  and  $E_{max}$  represent the energies bounding each energy bin. The equation now takes the form:

$$\bar{\sigma}_x^k(E_i) = \frac{1}{\sqrt{E_i^k}} * (E^{k+1} + E^k) * \frac{G(E^{k+1}, E_i^{k+1}) \sqrt{E^{k+1}} \sigma_x(E^{k+1}) + G(E^k, E_i^k) \sqrt{E^k} \sigma_x(E^k)}{2}, \quad (21)$$

where  $E_i^k$  is the average energy of channel  $i$  at time-bin  $k$ . The integrated cross section is calculated with the ENDF cross section and the resolution function at each time, and then divided by the width of the energy bin. There were 232 energy bins ranging from 0 to 14  $MeV$ , and 265 time bins ranging from 1 to 2000  $\mu s$ . Equation 21 was evaluated by incrementing through  $k$  for time, and then  $E_i^k$  was determined by the correlation between time and energy as shown in Equation 13.

## 2.3 Detectors

In a typical LSDS array, detectors are placed in and around the LSDS to monitor the neutron flux spectrum and the gamma rays produced from neutron interactions with the sample [7]. Flux monitors are not considered in the LSDS model proposed in this thesis due to the impact that they would have on the flux spectrum. There is no simple way to directly measure the neutron flux within the LSDS without disrupting

the flux profile.

The detector used in the model created for this thesis is a bismuth germanate (BGO) detector. It was modeled as a simplified cylindrical geometry representing an idealized germanium detector. A BGO detector was chosen for this task due to its high gamma capture efficiency and resolution [13]. Also, the materials that comprised the BGO detector would have a less significant impact than a detector that has low mass elements like hydrogen, which could disrupt the flux profile more.

## 2.4 Operation of the LSDS

1. There is a pulse of interrogating neutrons from the neutron source.
2. There is a short (approximately  $10 \mu s$ ) period of inelastic scattering, in which the average energy of the neutrons decreases from its starting energy down to about  $100 \text{ keV}$ . During this time, the energy of the incident neutrons cannot be determined, as they are losing energy (or gaining lethargy) in unpredictable amounts [10]. This results in a neutron energy spectrum that spans over two orders of magnitude, as seen in Figure 3. Since the neutron energy cannot be resolved, gamma rays detected during this time cannot be linked to a particular energy and no energy dependent cross section can be determined.

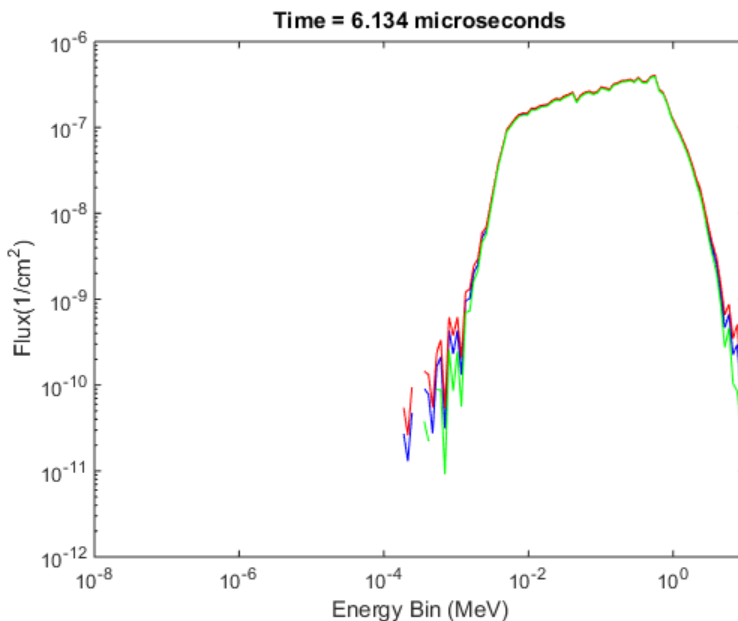


Figure 3: The neutron flux during inelastic scattering as output by MCNP. The time is the time after the pulse. The red and green lines represent the  $1 \sigma$  confidence interval.

3. The inelastic scattering period ends when the neutrons have an average energy of about  $100\text{ keV}$ , and they begin to lose energy through elastic scatters. Below this energy, the scattering becomes more consistent and as a result, the neutron spectrum narrows into a Gaussian distribution, which is described in detail in Section 4.4.2.

The more narrowed spectrum is shown in Figure 4.

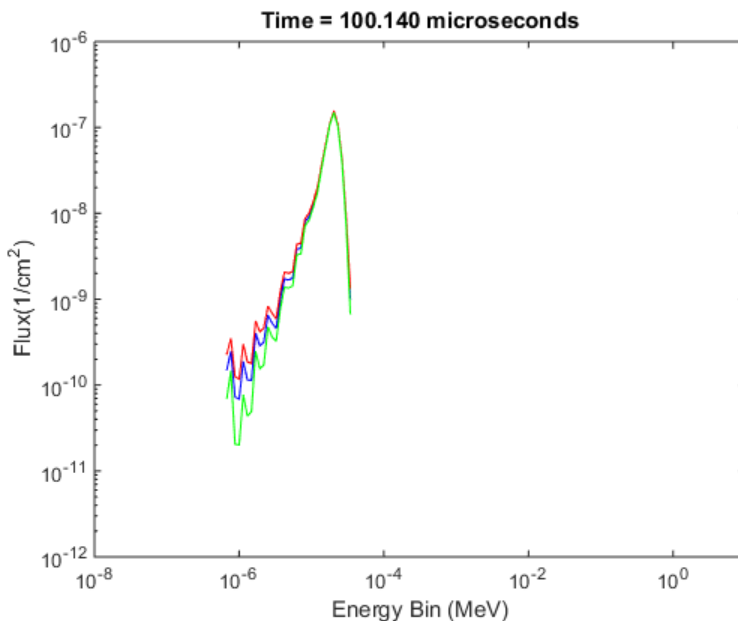


Figure 4: The neutron flux during elastic scattering. The time is the time after the pulse. The red and green lines represent the  $1\sigma$  confidence interval.

4. With a known neutron energy, gamma rays that are captured by the detector can be attributed to that particular energy.
5. The correlations described in Section 2.2 are used with the count rate to determine the cross section.

## 3 Monte Carlo Model

### 3.1 MCNP Basics

MCNP, which stands for “Monte Carlo N-Particle”, is a radiation transport simulation tool that models the movement of particles in a three-dimensional environment by using pseudo-random numbers and continuous-energy nuclear data to determine the sample from probability distributions for source particle birth, distance to collision,

and collision physics. [14]. It is generally considered the gold-standard, though it can be computationally expensive to use. The inputs data includes: the geometry of the system, the materials, sources, and the desired tally outputs. These tallies include various fluxes and energy depositions over time, which are the fluxes and gamma count rates when calculating the cross sections.

## 3.2 Extracting Data

The MCNP simulations computed F4:n tallies (neutron track length flux estimator in a volume) and F6:p tallies (photon energy deposited in a volume). F4:n outputs a scalar flux that is sorted into the defined energy bins and normalized by the number of source particles [15].

F6:p describes the energy deposited by photons within a volume, normalized by the number of source particles and the mass of the cell within the surface [15]. F6:p can be described by

$$F_6 = \left(\frac{\rho_a}{V\rho_g}\right) \int_V \int_t \int_E H(E) \sigma_t \Phi(r, E, t) dE dt dV, \quad (22)$$

where:  $\rho_a$  is the atomic density,  $\rho_g$  is the mass density, and  $H(E)$  is the heating response.

The tallies were extracted from MCNP into MatLab where they were sorted to be used in the analysis.

## 3.3 The LSDS in MCNP

The LSDS is physically a pile of lead bricks, but for the sake of simplicity, the LSDS was modeled as a solid lead structure that measured 152.4 *cm* along each side [2]. The model included two holes placed perpendicularly into the sides of the LSDS, one for the detector and sample, and one for the neutron source. The slot for the detector was 104.3 *cm* deep, and the slot for the source was 50.8 *cm* deep. The detector was modeled as a high purity beryllium germanate cylinder 7.63 *cm* long with a radius of 3.81 *cm*. The samples were typically modeled as a thin (25  $\mu\text{m}$  thick) foil wrapped around the detector. Several simulations were performed with the detector or sample in altered configurations. No physical structure was modeled for the neutron source.

All five faces of the LSDS exposed to air were covered in a 1 *mm* layer of high purity cadmium for shielding, and then covered in a layer of polyethylene doped to be 5 weight percent boron. Unless otherwise noted, each variation of the model involved 5.08 *cm* of borated polyethylene. The bottom face, which would be in contact with the ground, had a 1 *cm* steel plate placed beneath it, and then a layer of 1 *mm* thick

cadmium, and then another 1 *cm* steel plate. The plates were employed to prevent the cadmium from pressure welding to the lead from the weight of the LSDS.

The room around the LSDS was modeled as a standard laboratory room within the Radiation Center at Oregon State University [16]. The room is 20' by 20' (6 *m*), and has cinder-block walls that are 6" (15 *cm*) thick. The ceiling physically varied in height and thickness, but could conservatively be modeled as a 4" (10 *cm*) slab. The floor was modeled as a 2' (0.6 *m*) thick concrete slab. A simulated D-T fusion source was used as the neutron source, which yields 14.1 *MeV* neutrons.

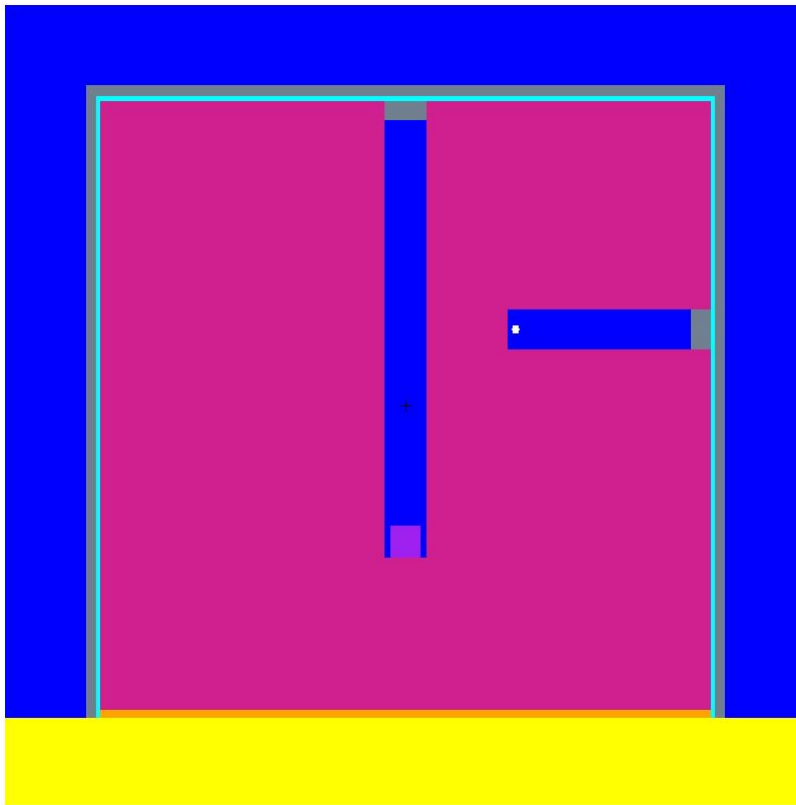


Figure 5: This is the full LSDS structure, as it was modeled in MCNP

## 4 Methods

### 4.1 Samples

Several cases were evaluated to see if the LSDS could be used with a variety of materials and for different mass samples. Unless otherwise specified, the sample was a foil encasing the detector, the neutron starting energy was 14.1 *MeV* and there were  $10^9$  source particles. 12 MCNP cases were completed to solve for cross sections:

1. Au-197
2. Au-197 ( $\times \frac{1}{5}$  mass)
3. Au-197 ( $\times 5$  mass)
4. Au-197 with the detector moved outside the volume of the LSDS
5. Au-197, with  $10^8$  source particles.
6. U-238
7. Ta (natural)
8. Ni (natural)
9. Ti (natural)
10. Cr (natural)
11. O-16
12. No sample

These materials were chosen as they have been identified as high-interest elements for further cross section development [1]. The natural compositions of Ni, Ta, Ti, and Cr were used to model the elements as they would be found in the structure of a reactor. Au-197 was chosen to be the standard due to having a fairly well-resolved radiative capture cross section.

The no sample problem was used as a filter for the other cases. The case without a sample contains the induced background that is associated with neutron interactions with the LSDS and the detector. If this case is subtracted from the other cases, the resulting net count rate should only represent neutron interactions with the sample. This filter was not applied to the moved detector case, as the detector would not be receiving the same induced background while placed outside the LSDS.

## 4.2 Determining the Cross Sections

Several factors must be calculated and taken into account to use the data from the LSDS. All of the values in Equation 23 must be known:

$$\sigma(E_i) = \frac{1}{\eta^x N^x} \frac{C_i^x}{F \phi_r(E_i) \Delta E_i}. \quad (23)$$

The “percent difference” was used to compare the calculated cross sections with the accepted ENDF cross sections. The percent difference is defined as

$$\% = \frac{X_1 - X_2}{\frac{X_1 + X_2}{2}} * 100, \quad (24)$$

in which:  $X_1$  is the exact or accepted value and  $X_2$  is the experimental value.

#### 4.2.1 ENDF Data

Data from the Evaluated Nuclear Data File (ENDF) database is used globally for nuclear data purposes. The data that would be derived from the use of the LSDS and Equation 23 would be equivalent to the ENDF broadened  $(n, \gamma)$  cross section,  $\bar{\sigma}_a$ , as a function of energy.

### 4.3 Poorly Resolved Region

At average energies greater than approximately  $100 \text{ keV}$ , the flux distribution cannot be used for cross section analysis; the energy spectrum spans several orders of magnitude, so no energy could be attributed to reactions within the sample. This means that time of flight methods would have to be used for cross sections at energies greater than  $100 \text{ keV}$ . The  $100 \text{ keV}$  cut-off represents a time of about  $10 \mu\text{s}$  after the initiation of the pulse.

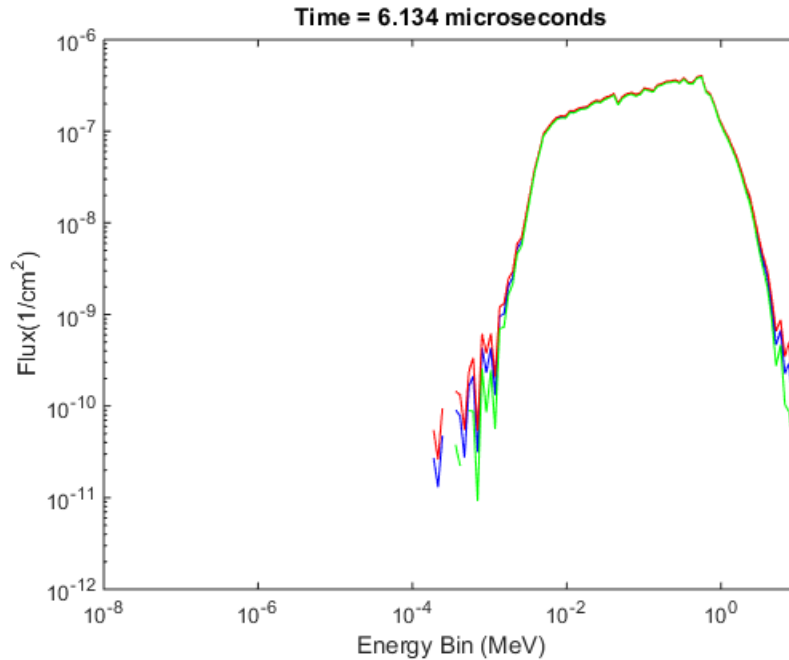


Figure 6: The width of the neutron spectrum is too great to made accurate determinations of a neutron energy for a calculated cross section.

## 4.4 Flux Profile

10  $\mu s$  after the pulse of neutrons, the flux can be described as:

$$\phi(t) = 2*10^{-16}*t^6 - 1*10^{-12}*t^5 + 3*10^{-9}*t^4 - 4*10^{-6}*t^3 + 0.0032*t^2 - 1.2945*t + 244.8, \quad (25)$$

in which:  $\phi$  is the neutron flux in  $cm^{-2}$  and  $t$  is the time after the pulse in  $\mu s$ .

This correlation has a residual of  $R^2 = 0.9955$ . The neutron flux here is the average of the neutron flux across all energy bins, which is also the highest relative flux intensity at that time. This is due to the normal distribution of the flux spectrum.

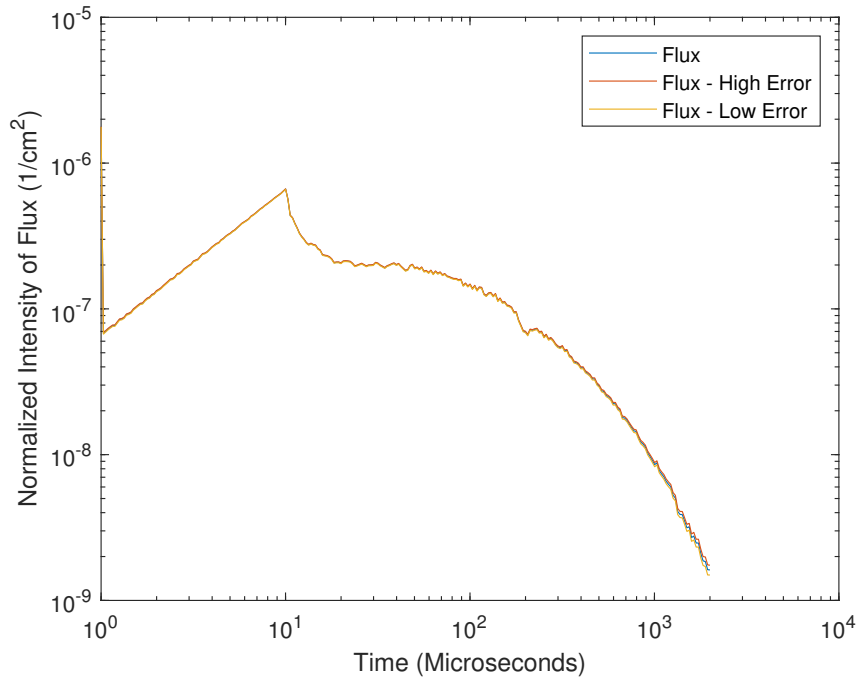


Figure 7: Uncertainty in neutron flux

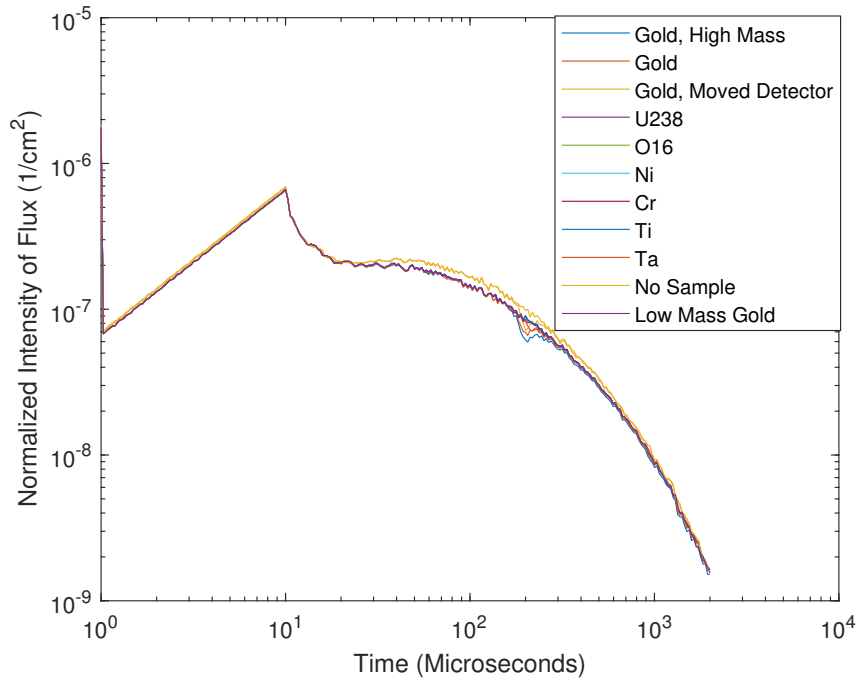


Figure 8: Neutron flux for different cases

In Figure 7, the uncertainty in the flux for the Au-197 case is shown. The uncertainty is  $\pm 1.38\%$  on average. In Figure 8, the flux profile for every simulation can is shown, including simulations that were used as proofs of concept and were not used for cross section analysis. The proof of concept cases were: no shielding, 1" (2.54 cm) of shielding, and vacuum conditions instead of the room and shielding. These models were simulated to demonstrate the impact of room return and different samples on the shape and magnitude of the flux profile. The biggest difference between any two points was between the vacuum boundary case and the moved detector case, which had a maximum percent difference of 65.99%. The average difference between all of the points of the various flux profiles and the flux profile defined by Equation 25 was 12.7%. If the vacuum, 1" shield, and no shield cases are removed from consideration, the average percent difference between the flux profiles is 5.56%. These proof-of-concept cases were not used for cross section development and were neglected in developing the flux profile.

In the design of the LSDS, the inclusion of contamination could have a significant impact on the flux profile [8]. The percent difference of 5.56% is relatively small, indicating that local changes may not have the same impact that impurities throughout the LSDS could have. None of the samples were notable poisons, and the inclusion of antimony, cadmium, or other highly absorptive materials has the potential to have a much greater effect.

#### 4.4.1 Determining $K$ and $t_0$

$K$  and  $t_0$  are parameters that are used to model the average energy within the LSDS as a function of time after the pulse of interrogating neutrons. If we start with the general slowing down equation, as discussed in Section 2.2,

$$du = \xi \Sigma_s v dt$$

rearranged and integrated from  $E_o$  to  $E$ , we have

$$t = \frac{\sqrt{2m_n}}{\xi \Sigma_s} \left( \frac{1}{\sqrt{E}} - \frac{1}{\sqrt{E_0}} \right). \quad (26)$$

Solving for  $E$ , or  $\bar{E}$  as the average energy, gives:

$$\bar{E} = \frac{K}{(t + t_0)^2}, \quad (27)$$

in which

$$K = \frac{2m_n}{\xi^2 \Sigma_s^2}, \quad (28)$$

and

$$t_0 = \frac{\sqrt{K}}{\sqrt{E_0}}, \quad (29)$$

where:  $m_n$  is the rest mass of a neutron,  $\xi$  is the average lethargy gain per collision, and  $\Sigma_s$  is the scattering cross section of the medium which is assumed to be constant for elastic scattering.

Putting the material properties of lead into the equation yields:

$$K = 171.6 \text{ keV} \cdot \mu\text{s}^2 \text{ and } t_0 = 0.265 \mu\text{s}. \quad (30)$$

This equation assumes an infinite medium of homogeneous materials. However, the LSDS contains air voids, detectors, samples, and a physically dissimilar room around it. All of these factors mean that the values determined analytically are not sufficient for determining the energy to a high degree of accuracy.  $K$  and  $t_0$  must be determined empirically through the use of MCNP. The energy of the highest relative neutron flux at each time-step from MCNP was fit to Equation (27).

Since

$$\bar{E} = \frac{K}{(t + t_0)^2},$$

and

$$t_0 = \frac{\sqrt{K}}{\sqrt{E_0}},$$

then  $K$  can be determined from the MCNP output by re-arranging these equations into:

$$K = \frac{E * t^2}{1 - \sqrt{\frac{E}{E_0}}}, \quad (31)$$

and then used to solve for  $t_0$  in Equation 29.  $K$  was determined by using the method of least squares to fit Equation 31 to the MCNP output seen in Figure 9 [17].

Ideally, the LSDS could be used for neutron energies up to 100  $keV$ , but a more complex equation may be needed to properly match the relationship between energy and time. The calculated energy and the MCNP output did not converge until approximately 250  $eV$ . The average difference between the MCNP output energy and the calculated energy in the energy range that is less than 250  $eV$  is 2.8%, indicating good agreement. The difference between the two is shown in Figure 9. The same linear fit could be applied to accommodate the higher energies, but the average difference between the MCNP output and the log-log fit becomes 190% if the energy is evaluated from 100  $keV$  and below.

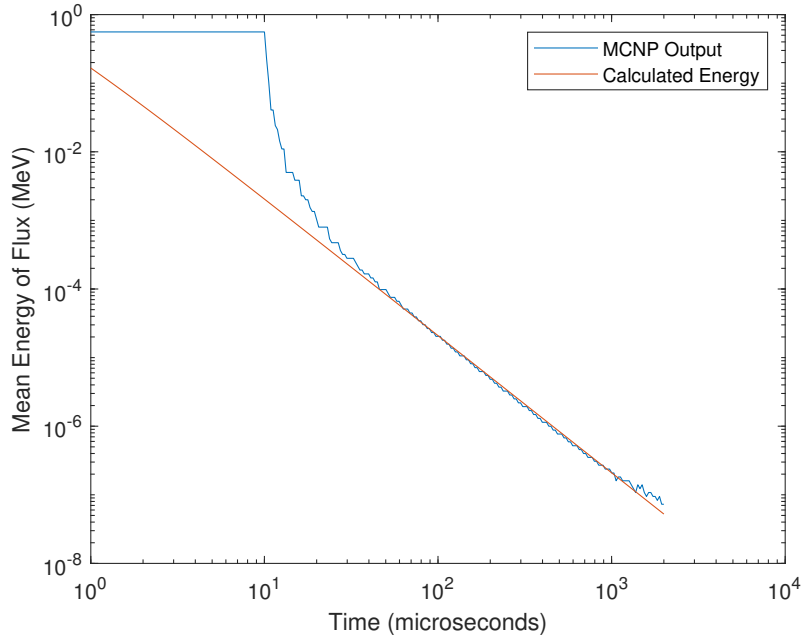


Figure 9: Comparing the calculated energy to the MCNP output.

The values of  $K$  range between  $208.84 \text{ keV} \cdot \mu\text{s}^2$  for the O-16 case and  $217.72 \text{ keV} \cdot \mu\text{s}^2$  for the moved detector case. The final value used for all cases was:

$$K = 209.61 \pm 3.51 \text{ keV} \cdot \mu\text{s}^2, \quad (32)$$

and  $t_0$  was determined to be

$$0.1224 \pm 0.0010 \mu\text{s}. \quad (33)$$

#### 4.4.2 The Resolution Function

After the average energy of the flux spectrum is below  $100 \text{ keV}$ , the flux distribution becomes a normal (Gaussian) distribution centered on the average energy. Since the distribution is normal, the average neutron energy is also the mode of the distribution, and therefore the energy of the neutron that is most likely to be the cause of a radiative capture. The average energy of the flux at each time-step was determined by using the energy bin that contained the maximum of the energy dependent flux distribution at that time-step. The theoretical resolution of the flux was analytically derived by Bergmann et al. [9]. The full width at half maximum (FWHM) was found to be:

$$G = \frac{dE}{E_{FWHM}} = [8 \log(2) \left( \frac{8}{3A} + 4D_0 \frac{E}{E_0} + \frac{kT}{E} \right)]^{\frac{1}{2}}, \quad (34)$$

which, for lead, gives

$$\frac{dE}{E}_{FWHM} = [0.720 + \frac{0.140}{E} + 6.59 * 10^{-5} E]^{\frac{1}{2}}. \quad (35)$$

However, the analytical solution is not always the most accurate solution, as it does not include the presence of the sample, detector, or the room around the LSDS. For these reasons, more accurate resolutions were derived empirically for LSDSs in the form of

$$\left(\frac{dE}{E}\right)_{FWHM} = [0.0835 + \left(\frac{0.128}{E}\right) + 3.05 * 10^{-5} E]^{\frac{1}{2}}, \quad (36)$$

which is the resolution function used by Danon et al. in the RPI LSDS [11]. It is also used for the model of this LSDS.

## 4.5 Determining Count Rate

The count rate for gamma interactions in the BGO detector was computed using the F6:p tally as discussed in Section 3.2. Once the output was normalized by the number of source particles, a filter was applied to the results. The filter was a case simulated in MCNP that contained no sample, so any photons would be from interactions with the detector, air, and lead. This filter was subtracted from the other cases, which would theoretically just leave the photons emitted by the sample. Other background was not considered, as the detector is insulated by at least 28 *cm* of lead on every side.

## 4.6 Determining the Flux Normalization Factor

The flux normalization factor is a method of “tuning” the LSDS. This is used to account for the LSDS parameters that need to be determined empirically.

The flux normalization factor was originally determined for the Au-197 case alone, and was then going to be used for all cases. However, when the normalization factor was determined for the other cases, some of the factors differed by more than an order of magnitude. To account for this, two generalized flux normalization factors were developed; one was for the higher atomic mass samples, and other for the lower atomic mass samples. The results of this are displayed in Table 1. Danon et al. established precedence for using one flux normalization factor for multiple samples [11]. The intent of the averaged normalization factors is to calculate a normalization factor that could be used for isotopes with unknown cross sections, using the method

developed by Danon et al.

Sample	F
Au-197	1.3129E-22
Au-197, low mass	5.9624E-22
Au-197, high mass	4.9825E-23
Au-197, moved detector	1.5528E-24
Au-197, $\frac{1}{10}$ source particles	1.3497E-22
U-238	4.8172E-22
Ta	1.0789E-22
Ni	3.2532E-21
Ti	4.1896E-21
Cr	2.6383E-21
O-16	9.1638E-17
High A Average	2.40E-22
Low A Average	3.36E-21

Table 1: Normalization factor for each sample

The trend that is apparent is the difference in the normalization factor between high atomic number samples, and low atomic number samples. For the same geometry and similar number of atoms, Au-197, U-238, and elemental Ta have an average normalization factor of  $2.40\text{E-}22$ . This is a percent difference of 59%, 67%, and 76% for Au-197, U-238, and Ta, respectively. Despite the lower number of atoms, the low mass Au-197 sample is within 85% of the average. The moved detector case appears to be an outlier, until the change in solid angle is considered. Solid angle and intrinsic detector efficiency describe  $\eta$  in Equation 23 [18]. Dividing the average normalization factor by this solid angle, with the intrinsic efficiency of the detector remaining constant, yields a normalization factor of  $3.11\text{E-}22$ , a percent difference of 26% from the high atomic mass average. This division occurs as a part of the cross section calculation process, but it is described here to show the appropriateness of applying the high atomic mass normalization factor to the moved detector case. The high mass Au-197 sample also appears to be an outlier, but the increase in  $N$  can be considered the same way the decrease in  $\eta$  is for the moved detector. If the larger  $N$  is considered, the effective  $F$  becomes  $2.4625\text{E-}22$ , which is a percent difference of only 2.5% from the high atomic mass average.

For Cr, Ti, and Ni, the average normalization factor is  $3.36\text{E-}21$ , with respective differences of 24%, 22%, and 3.2%. O-16, as the sample with the lowest atomic mass, has a factor that is at least three orders of magnitude larger than all the other samples, so it had no other sample that could be placed in a group with it.

## 5 Results

Now that the variables needed to calculate the cross section are defined, the cross section can be computed from

$$\sigma(E_i) = \frac{1}{\eta^x N^x} \frac{C_i^x}{F \phi_r(E_i) \Delta E_i}. \quad (37)$$

The error and uncertainty in the computed cross section arise from the combination of the uncertainty from MCNP and the resolution function of the neutron spectrum at each time-step.

The results of the various test problems were analyzed in a variety of ways:

Method 1: The normalization factor was calculated for every time-step for the energy bin that includes 411 keV, which is the channel containing the characteristic decay gamma from Au-198. This normalization factor was then used in the cross section calculation, and gave back an exact match for the broadened cross section. This was expected and served as a verification check of self-consistency.

Method 2: The normalization factor calculated using Method 1 was averaged across each time-step, and the average flux normalization factor was used to calculate the cross section of Au-197. The same count rate that was used to solve for  $F$  was used to solve for the cross section.

Method 3: The normalization factor was calculated for each sample, and an average factor was developed for both the high and the low atomic mass samples. The appropriate flux normalization factor was used to evaluate the cross section of the cases.

The high atomic mass cases were:

1. Au-197
2. Au-197 ( $\frac{1}{5}$  original mass)
3. Au-197 (x5 original mass)
4. Au-197 with the detector moved outside the volume of the LSDS
5. Au-197, with  $10^8$  source particles
6. U-238
7. Tantalum (natural)

and the low atomic mass cases were:

8. Nickel (natural)
9. Titanium (natural)
10. Chromium (natural)

The normalization factor for O-16, Case 11, was not grouped with other samples due to its flux normalization factor being more than 3 order of magnitude greater than the normalization factor for any other sample. In computing the O-16 cross section, an O-16 specific normalization factor was used.

## 5.1 Cross Sections

The plots below show comparisons of the resulting energy-dependent cross sections from the LSDS simulation and the broadened ENDF cross section for each case. In several of the plots, the gaps that appear in the ENDF broadened cross section are due to the cross section of a resonance peak exceeding the boundaries of the figure.

### 5.1.1 Case 1, Au-197

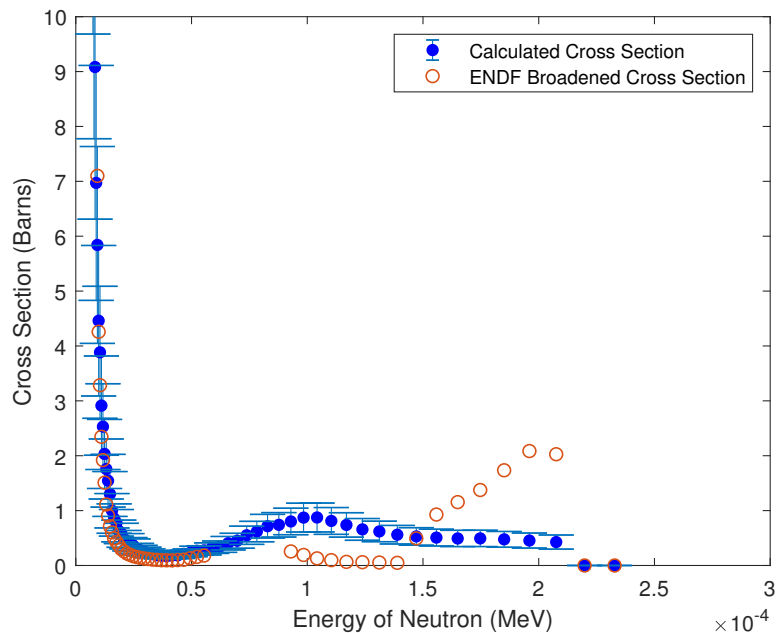


Figure 10: Cross section of Au-197 in the 100s of  $eV$  range

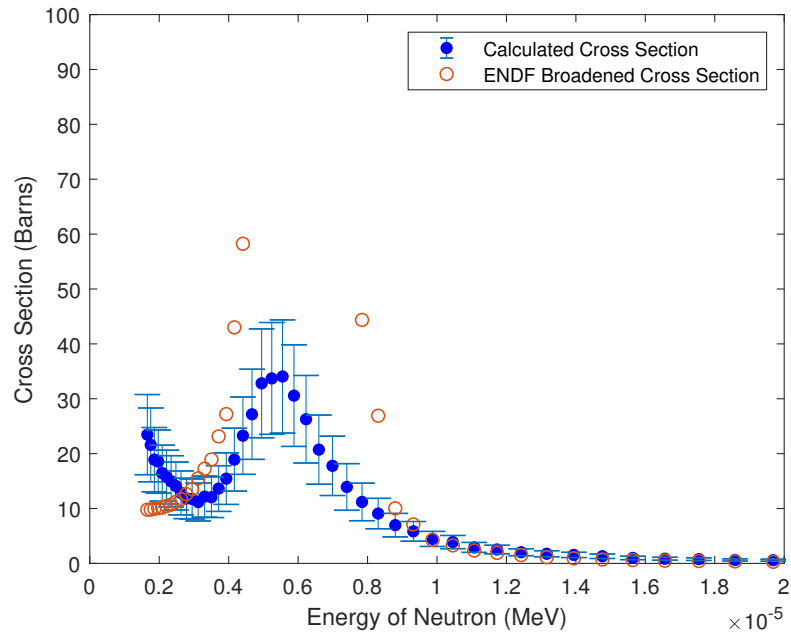


Figure 11: Cross section of Au-197 in the  $eV$  range

### 5.1.2 Case 2, Low Mass Au-197

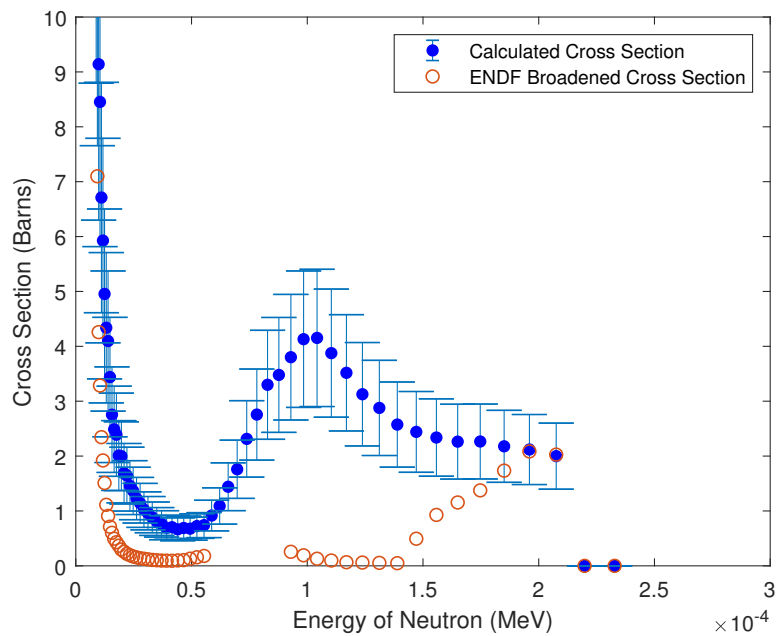


Figure 12: Cross section of low mass Au-197 sample in the 100s of  $eV$  range

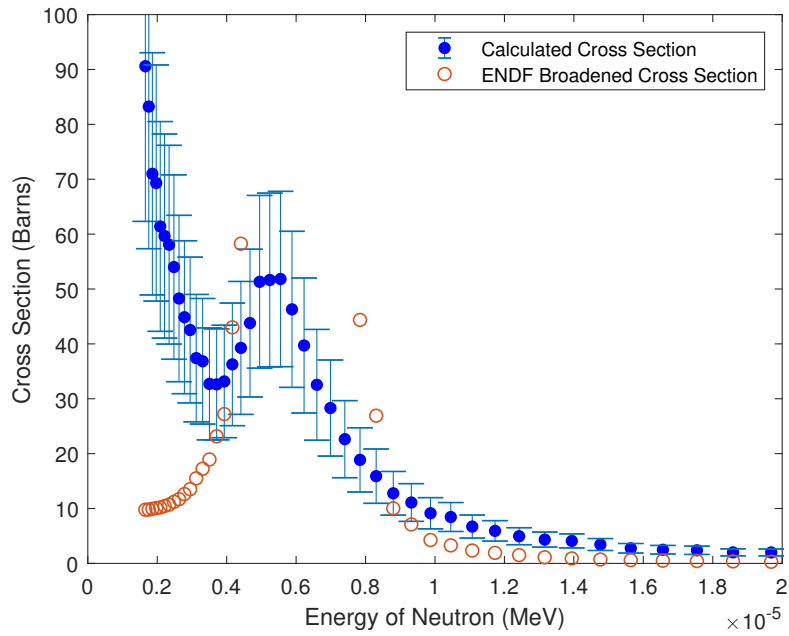


Figure 13: Cross section of low mass Au-197 sample in the  $eV$  range

### 5.1.3 Case 3, High Mass Au-197

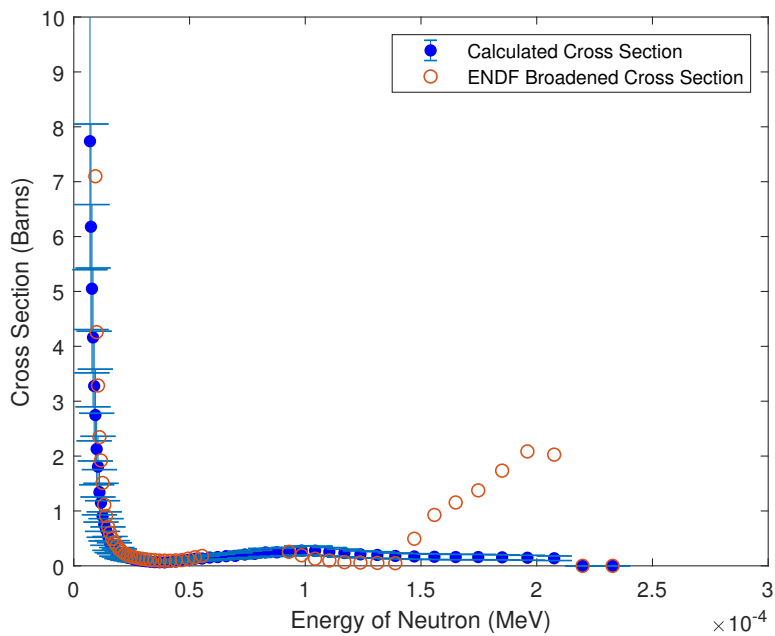


Figure 14: Cross section of high mass Au-197 sample in the 100s of  $eV$  range

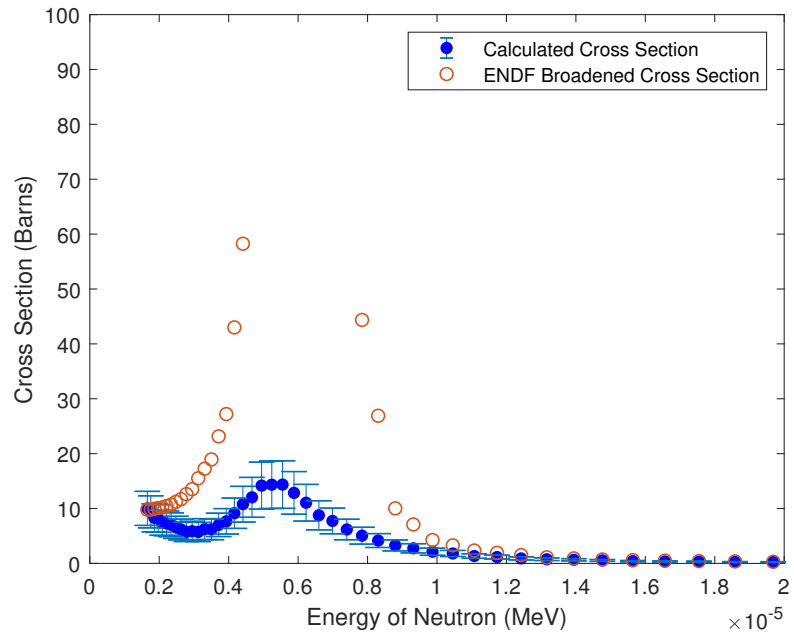


Figure 15: Cross section of high mass Au-197 sample in the  $eV$  range

### 5.1.4 Case 4, Moved Detector, Au-197

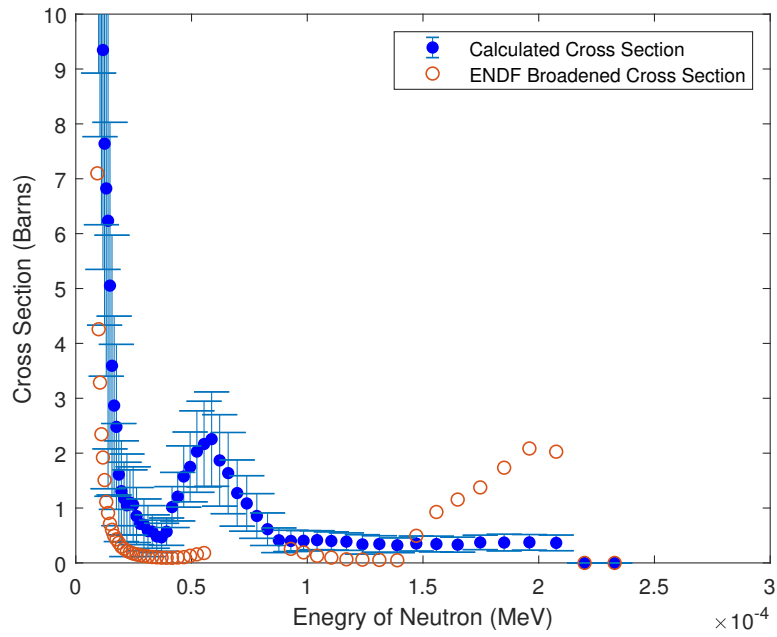


Figure 16: Cross section of Au-197 sample in the 100s of eV range, with the detector outside the LSDS

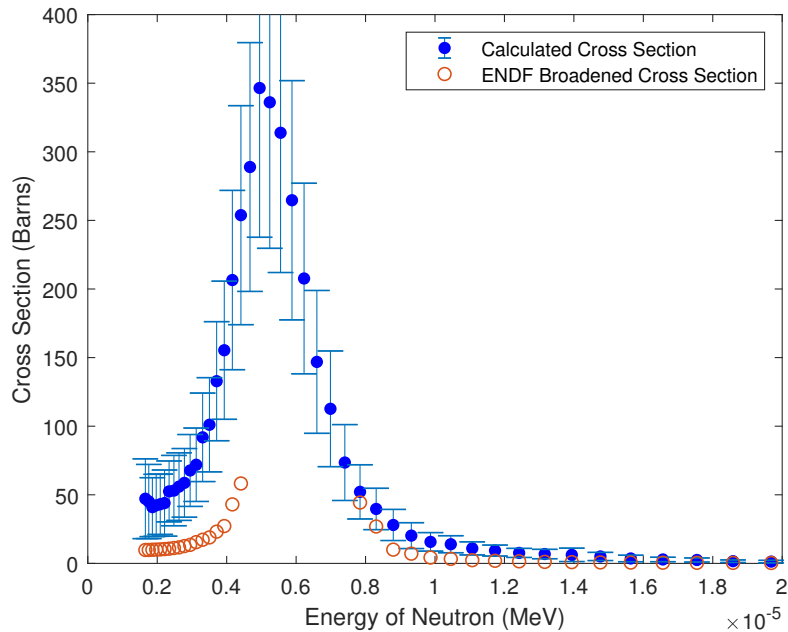


Figure 17: Cross section of Au-197 sample in the  $eV$  range, with the detector moved outside the LSDS

In all of the Au-197 cases, the calculated cross section did not reach the same magnitude as the ENDF broadened cross section in the resonance region. In each Au-197 case, the calculated cross section began following the broadened cross section around  $50 eV$ , but could not reach the approximately  $4000 b$  peak. Instead, the calculated peak was as high as 2.5 to 8.8% of the broadened cross section peak, depending on the case. The moved detector had the highest peak, reaching  $348 b$ . At higher energies, the calculated cross section followed a trend more similar to an averaged cross section over the resonance region. This indicates that further broadening the cross section could allow them to have better agreement. The difference between the calculated cross section and the ENDF broadened cross section is shown in Table 3.

The increase in the calculated cross section beginning between 3 and 4  $eV$  is due to shielding from the detector. The increase is from reactions occurring in the detector, which is overshadowing the reactions from the sample due to the much higher mass of the detector. This is shown by the lack of increase from the moved detector case, shown in Figure 17, as the detector is exposed to a lower intensity neutron flux.

It was speculated that there were not enough absorption reactions occurring in the MCNP model, and that more particles could potentially increase the cross section to match the broadened cross section. This was tested by comparing the original case with  $10^9$  particles to a lower fidelity case with  $10^8$  particles. The theory would be

proved true if the resonance was less defined for the  $10^8$  source particle case. The average percent difference between the calculated cross sections is 8.3%, and the maximum percent difference between the cross sections is 28%. This indicates that more particles could allow for more defined resonances. However, as a conservative thought experiment, assume that the magnitude of the resonance increases by 28% for every increase by an order of magnitude of particles. For the calculated resonance peak to increase by a factor of 100 to match the broadened resonance peak, it would require the source strength to increase by 19 orders of magnitude. This is not practical to implement using MCNP. The calculated cross section for the low source particle case is shown in Figures 18 and 19.

### 5.1.5 Case 5, Au-197 with $10^8$ Source Particles

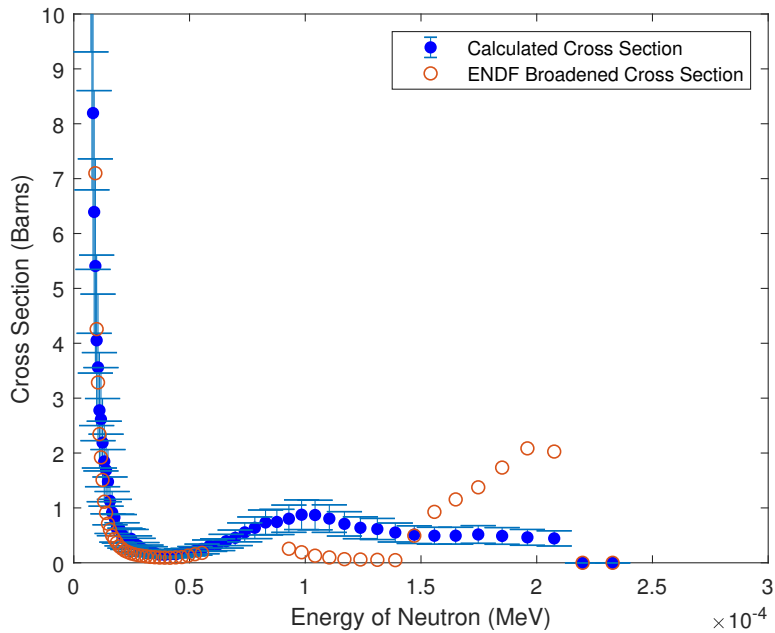


Figure 18: The cross section of Au-197 using  $10^8$  source particles in the 100s of  $eV$  range

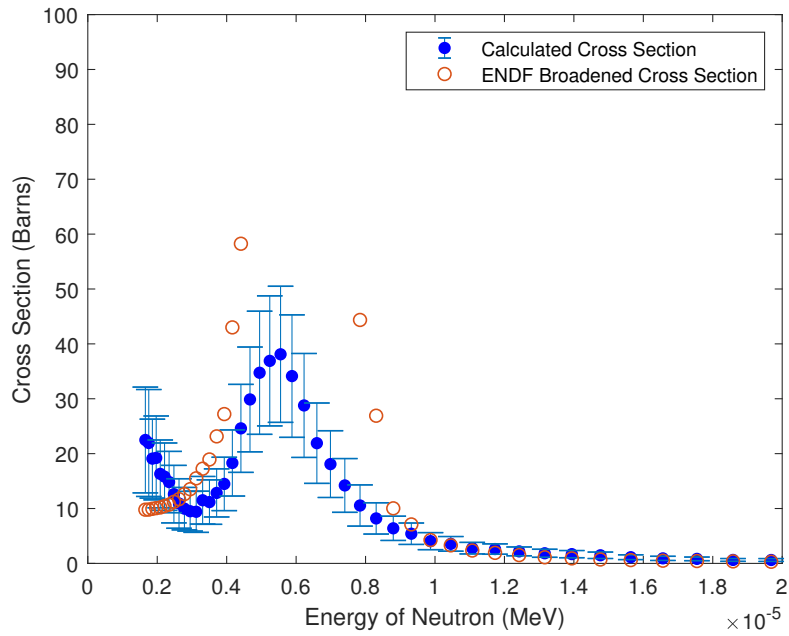


Figure 19: The cross section of Au-197 using  $10^8$  source particles in the  $eV$  range

### 5.1.6 Case 6, U-238

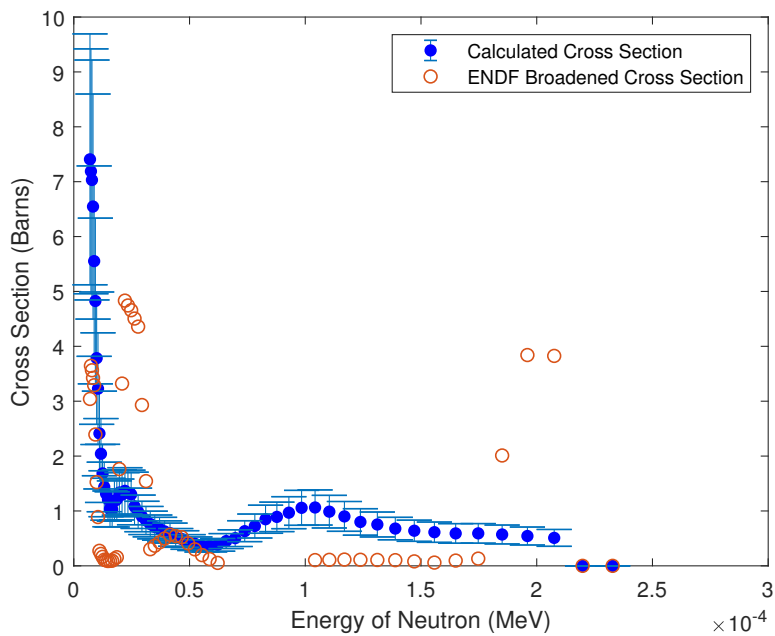


Figure 20: The cross section of U238 in the 100s of  $eV$  range

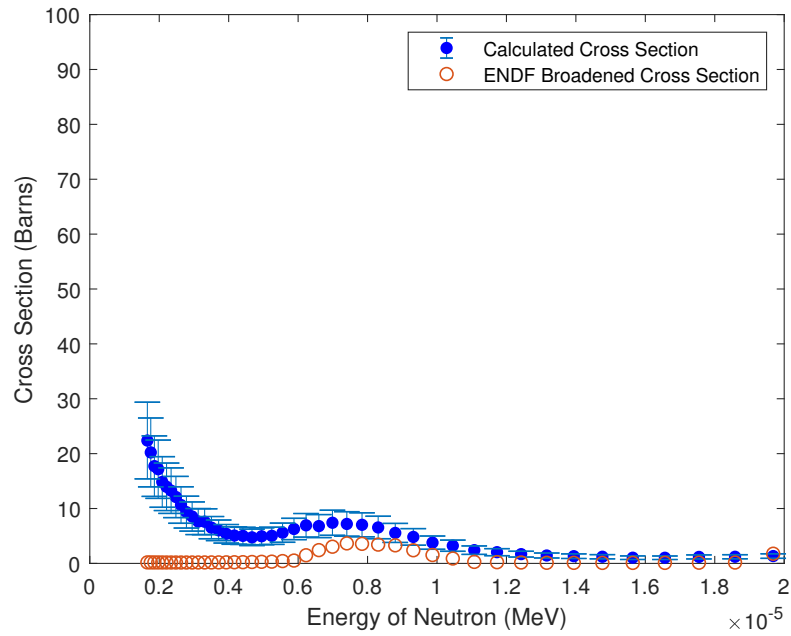


Figure 21: The cross section of U238 in the  $eV$  range

The U-238 case had the greatest difference between the calculated and broadened cross sections. The influence of the detector is shown in the sinusoidal shape between 50 and 100  $eV$ , and the increase around 4  $eV$ .

### 5.1.7 Case 7, Tantalum

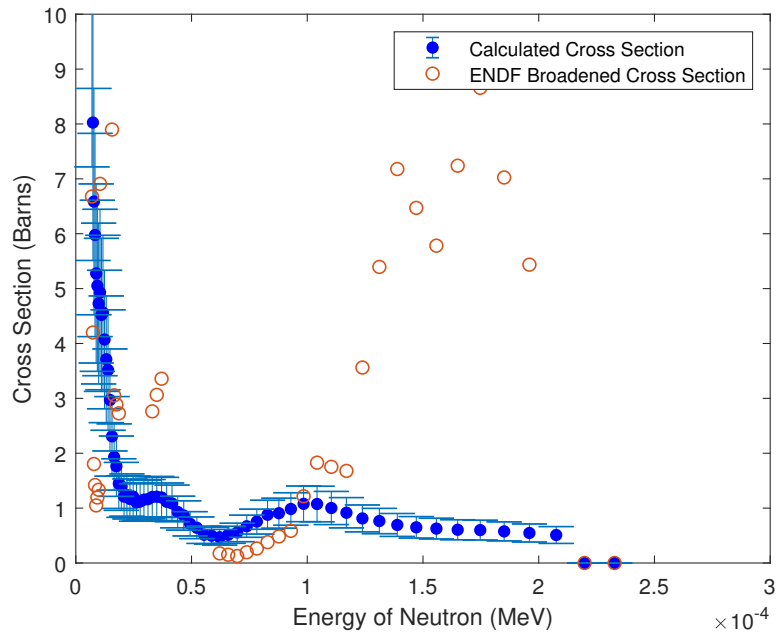


Figure 22: The cross section of natural tantalum in the 100s of  $eV$  range

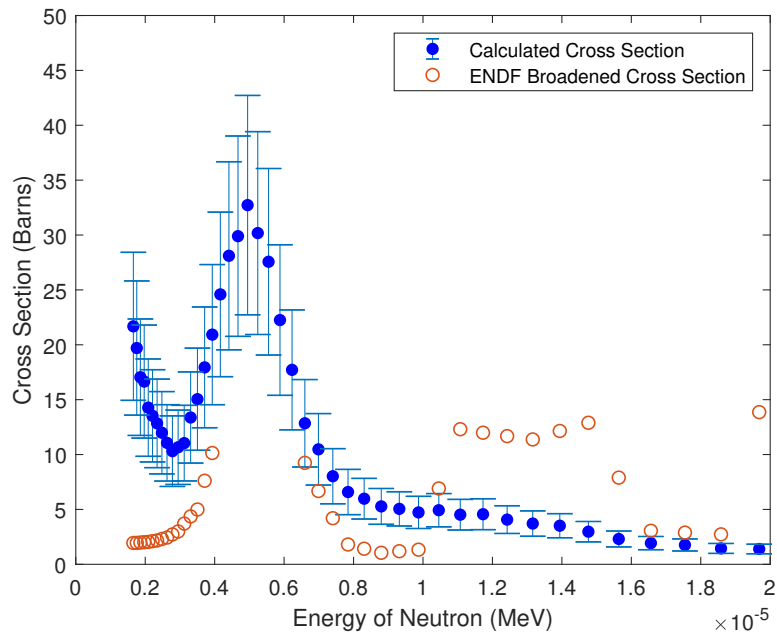


Figure 23: The cross section of natural tantalum in the  $eV$  range

In Figure 23, the calculated cross section for tantalum does respond to the peak around 6 eV. However, in Figure 24, the degree to which the the calculated cross section did not agree with the ENDF broadened cross section is shown. The average degree of agreement is shown in Table 3.

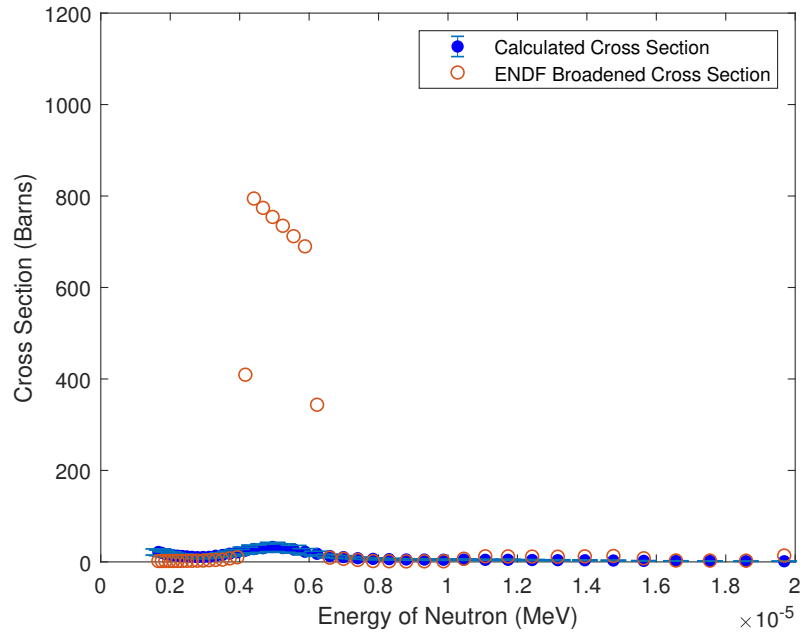


Figure 24: The largest resonance peak of tantalum only caused a small response

### 5.1.8 Case 8, Nickel

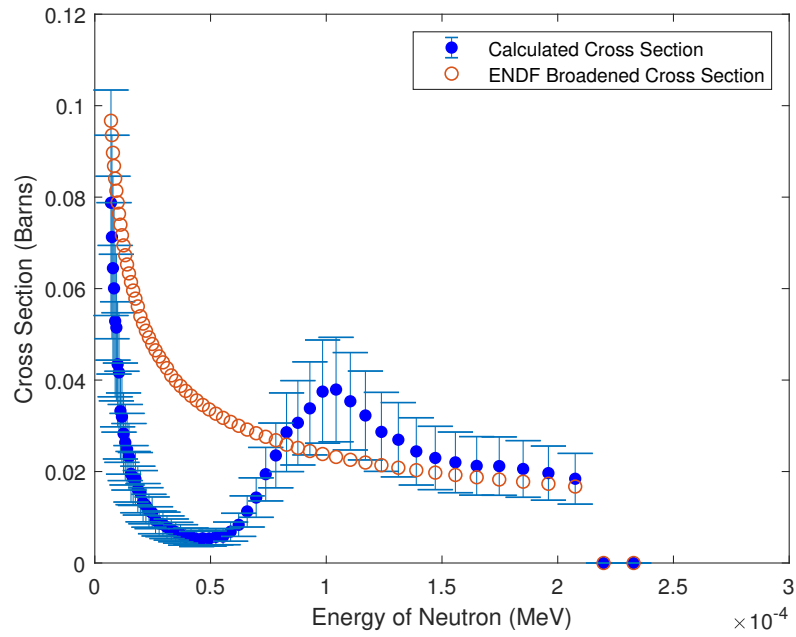


Figure 25: The cross section of nickel in the 100s of  $eV$  range

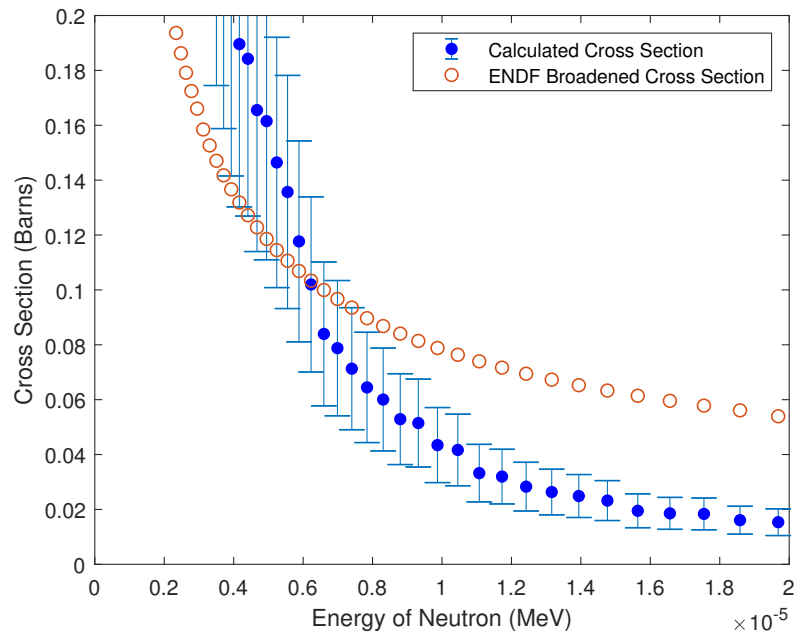


Figure 26: The cross section of nickel in the  $eV$  range

### 5.1.9 Case 9, Titanium

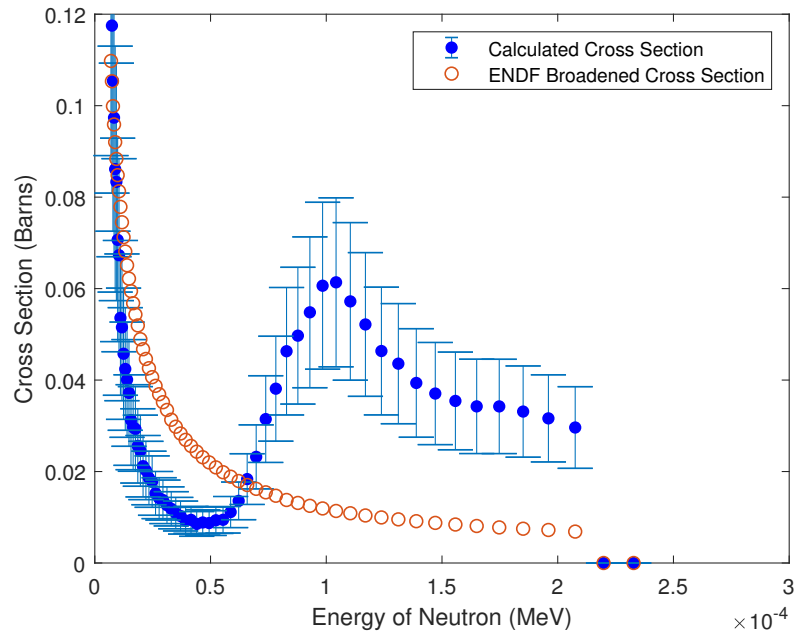


Figure 27: The cross section of titanium in the 100s of  $eV$  range

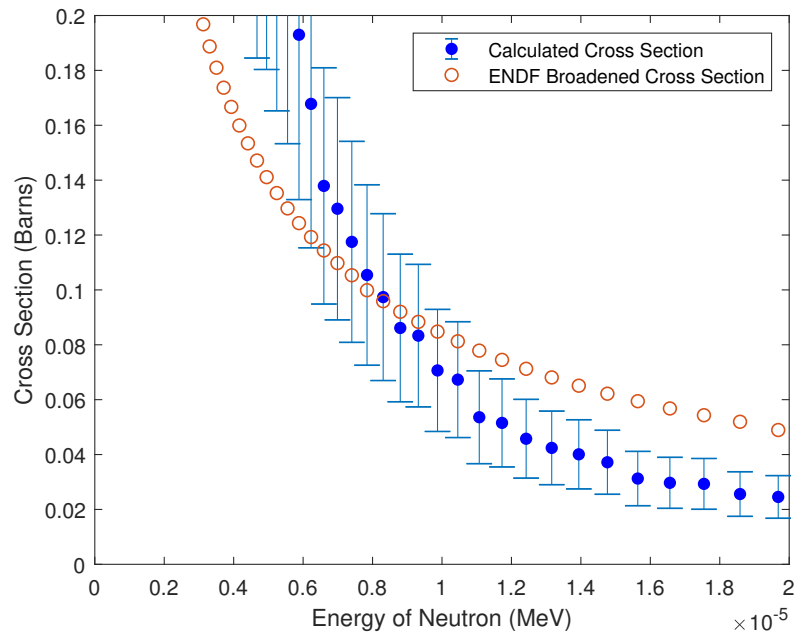


Figure 28: The cross section of titanium in the  $eV$  range

### 5.1.10 Case 10, Chromium

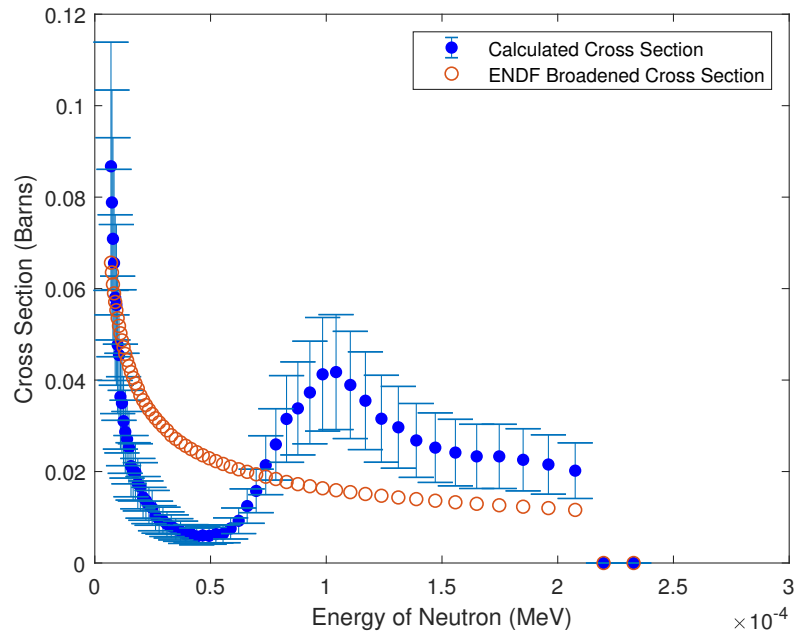


Figure 29: The cross section of chromium in the 100s of  $eV$  range

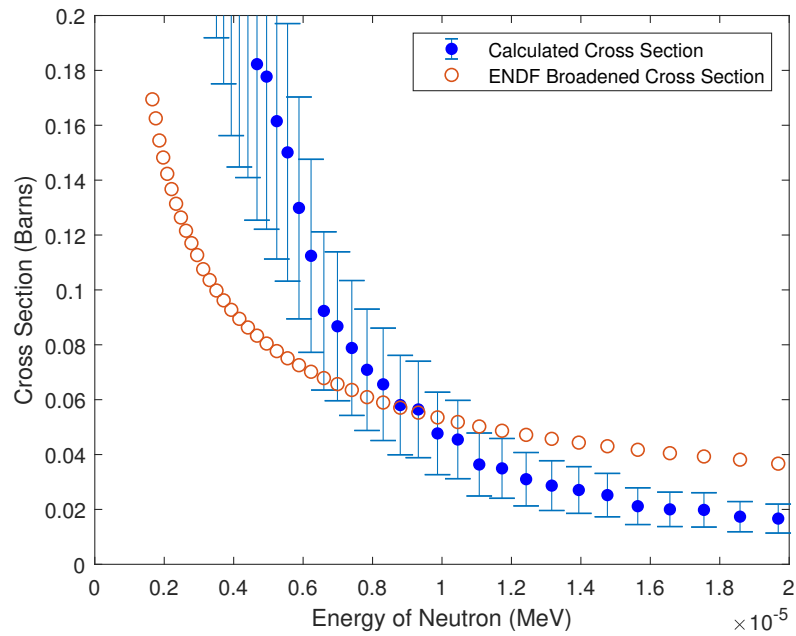


Figure 30: The cross section of chromium in the  $eV$  range

In all of the low atomic mass cases, the impact of the detector appears as the sinusoidal shape between 50 and 100 eV. The discrepancy between the broadened cross section and the calculated in the eV range is also likely due to the detector.

### 5.1.11 Case 11, O-16

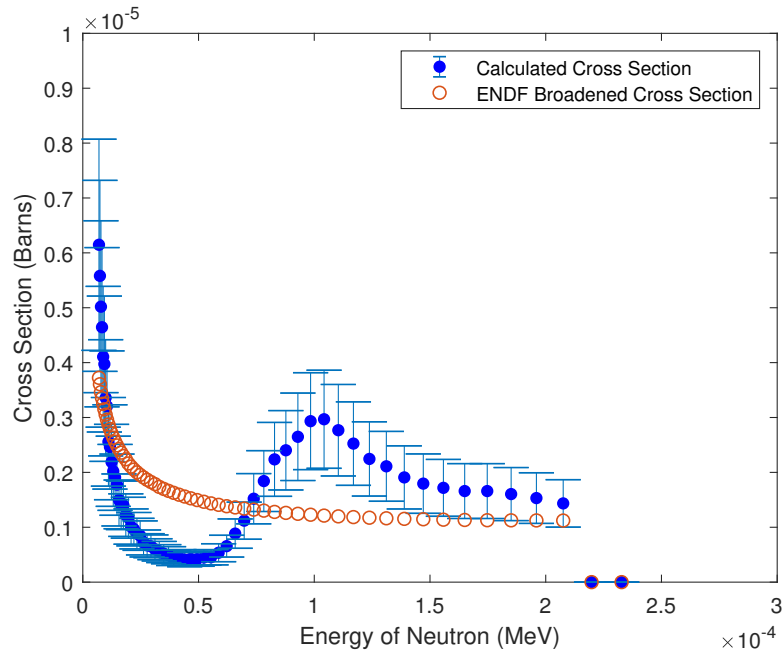


Figure 31: The cross section of O-16 in the 100s of eV range

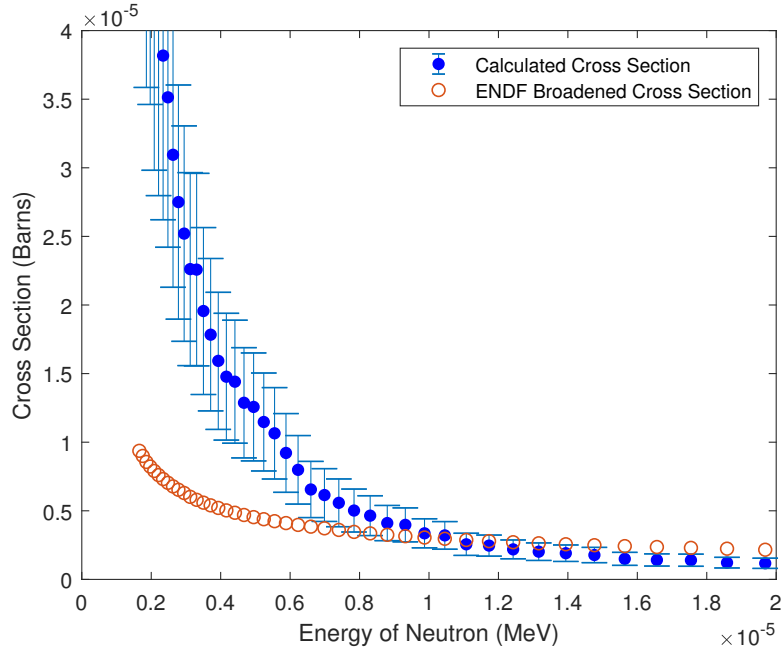


Figure 32: The cross section of O-16 in the  $eV$  range

The O-16 case displayed similar errors as the low atomic mass cases, with the sinusoidal shape between 50 and 100  $eV$  and the sharp increase around 5  $eV$ .

### 5.1.12 Tabulated Results

The uncertainty columns are the average uncertainty of the calculated cross section value, within the specified energy range. The uncertainty values are in Table 2. The energy range that each column is evaluated over correlates to the energy ranges shown in the figures. The percent difference table represents the average percent difference between the calculated cross section and the broadened ENDF cross section, within the specified energy range. The percent difference values are in Table 3.

Sample	100s of eV range (%)	eV range (%)
Au-197	27.7	29.2
Au-197, low mass	28.0	29.4
Au-197, high mass	27.5	29.0
Au-197, moved detector	41.7	44.1
Au-197, $\frac{1}{10}$ source particles	32.9	35.2
U-238	28.0	29.5
Ta	27.8	29.3
Ni	28.1	29.5
Ti	28.1	29.5
Cr	28.1	29.5
O-16	28.1	29.5

Table 2: Uncertainty of each sample

Sample	100s of eV range (%)	eV range (%)
Au-197	62.0	66.1
Au-197, low mass	274	301
Au-197, high mass	43.3	48.4
Au-197, moved detector	295	309
Au-197, $\frac{1}{10}$ source particles	69.4	70.4
U-238	404	2990
Ta	105	247
Ni	47.3	80.0
Ti	30.4	101
Cr	34.0	135
O-16	36.3	180

Table 3: Percent difference of each sample

## 5.2 Shortcomings

The sinusoidal shape seen in many of the cases is likely from a 750  $b$  resonance peak of germanium around 10  $eV$ . This indicates that the filter case did not function as intended. Also, the lack of well-defined resonances is problematic. However, the calculated cross sections within the resonance region could likely be improved through a number of methods.

1. Update filter case - Simulate the filter case again to ensure that it is properly implemented, and then ensure it is being incorporated properly.

2. Higher particle count - More particles would lead to further reduction in uncertainty and an improvement in the flux normalization factor.
3. Move the detector - the case in which the detector was moved showed the best response to a resonance peak, and likely had a large error due to a poorly fit flux normalization factor.
4. Improved detector array - A more sophisticated detector array could help to distinguish events and reduce uncertainty.

## 6 Conclusion

The principles of the LSDS to produce a consistent flux spectrum have been verified. The ability of the LSDS to produce a similar neutron flux despite the inclusions of a wide range of materials and differing detector geometries affirms the capacity for the LSDS to be used for cross section analysis.

The LSDS does show potential to fill in the gaps that exist in the current nuclear data repository. However, higher fidelity simulations are required to verify whether the LSDS can truly address the gaps that exist. The errors that are currently in the model will need to be systematically explored. In general, the calculated cross sections and the broadened ENDF cross sections do not agree yet, but the application of the suggested improvements could allow for better results.

### 6.1 Future Work

The direction of future efforts will be to change the MCNP input to focus more on energy bins in the higher energy region in the form of shorter simulations that end at the  $\frac{1}{v}$  region, which should allow for less computationally expensive results. The relationship governed by  $K$  and  $t_0$  should be re-evaluated to increase the energy that the relationship can modeled at accurately. A further continuation of this work would be to analyze the reactions besides  $(n, \gamma)$ , such as  $(n, \alpha)$  or fission cross sections.

## References

- [1] L. BERNSTEIN, “Nuclear Data Needs and Capabilities for Applications,” .
- [2] T. PALMER, “Reducing the Uncertainty in Energy-Dependent Nuclear Data Designing and Deploying a Next-Generation Lead Slowing Down Time Spectrometer,” (2015).
- [3] L. J. H. JAMES J. DUDERSTADT, *Nuclear Reactor Analysis* (1976).

- [4] F. TOVESSON, “Uncertainty Quantification in Fission Cross Section Measurements at LANSCE,” (2014).
- [5] C. MOBLEY, “The construction of a Fermi neutron chopper for cross section measurements,” (1966).
- [6] E. FERMI, “A Thermal Neutron Velocity Selector and Its Application to the Measurement of the Cross Section of Boron,” (1947).
- [7] Y. DANON, “Measurements with the high flux lead slowing-down spectrometer at LANL,” (2007).
- [8] D.ROCHMAN, “Characteristics of a lead slowing-down spectrometer coupled to the LANSCE accelerator,” (2005).
- [9] A. BERGMAN, “A Neutron Spectrometer Based on Measuring the Slowing-Down Time of Neutrons in Lead,” (1955).
- [10] Y. DANON, “Measurements with a Lead Slowing-Down Spectrometer,” (2015).
- [11] Y. DANON, “Fission Cross-Section Measurements of  $^{247}\text{Cm}$ ,  $^{254}\text{Es}$ , and  $^{250}\text{Cf}$  from 0.1 eV to 80 keV,” (1991).
- [12] S. SHANBHAG, “Numerical Integration (Quadrature),” .
- [13] “Bismuth Germanate Scintillation Material,” (2016).
- [14] J. T. GOORLEY, *MCNP6 User’s Manual* (2015).
- [15] E. HUSSEIN, “Monte Carlo Particle Transport with MCNP,” .
- [16] S. REESE, “Personal Correspondence,” (2016).
- [17] S. MILLER, “The Method of Least Squares,” (2003).
- [18] N. TSOULFANIDIS, *Measurement and Detection of Radiation* (1995).

